Geochemistry, Geophysics, Geosystems

RESEARCH ARTICLE
10.1029/2018GC007861

Anomalously Deep BSR Related to a Transient State of the Gas Hydrate System in the Western Black Sea

S. Ker[1], Y. Thomas[1], V. Riboulot[1], N. Sultan[1], C. Bernard[1,2], C. Scalabrin[1], G. Ion[3], and B. Marsset[1]

[1]Ifremer, REM-GM, Plouzané, France, [2]ENSTA Bretagne, Brest, France, [3]GeoEcoMar, Bucharest, Romania

Key Points:
- There is a discrepancy between observed BSR depth and theoretical steady state base of gas hydrate stability zone
- The transient state of the hydrate system is due to excess pore pressure related to hydrate dissociation
- BSR depth is used to derive maximum excess pore pressure at the base of the gas hydrate stability zone

Correspondence to:
S. Ker,
stephan.ker@ifremer.fr

Citation:
Ker, S., Thomas, Y., Riboulot, V., Sultan, N., Bernard, C., Scalabrin, C., Ion, G., & Marsset, B. (2019). Anomalously deep BSR related to a transient state of the gas hydrate system in the western Black Sea. *Geochemistry, Geophysics, Geosystems*, *20*, 442–459. https://doi.org/10.1029/2018GC007861

Received 26 JUL 2018
Accepted 27 DEC 2018
Accepted article online 3 JAN 2019
Published online 23 JAN 2019

Abstract A comprehensive characterization of gas hydrate system offshore the western Black Sea was performed through an integrated analysis of geophysical data. We detected the bottom-simulating reflector (BSR), which marks, in this area, the base of gas hydrate stability. The observed BSR depth does not fit the theoretical steady state base of gas hydrate stability zone (BGHSZ). We show that the disparity between the BSR and predicted BGHSZ is the result of a transient state of the hydrate system due to the ongoing reequilibrium since the Last Glacial Maximum. When gas hydrates are brought outside the stability zone due to changes in temperature and sea level, their dissociation generates an increase in interstitial pore pressure. This process is favorable to the recrystallization of gas hydrates and delays the upward migration of the hydrate stability zone explaining the anomalously deep BSR. The BSR depth, which is commonly used to derive geothermal gradient values by assuming steady state conditions, is used here to derive the maximum excess pore pressure at the BGHSZ. Derived excess pore pressure values of 1–2 MPa are probably the result of the low permeability of hydrate-bearing sediments. Higher pore pressure values derived at the location of a fault system could cause hydrofracturing enabling the free gas to cross the gas hydrate stability zone and emerge at the seafloor, forming the flares observed in close vicinity to where the shallow gas hydrates were sampled.

1. Introduction

Since the first recovery of gas hydrates within marine sediments at the beginning of the 1970s and decades of scientific investigations (Ginsburg, 1998; Yefremova & Zhizhchenko, 1974), the Black Sea is nowadays considered to contain large amounts of hydrate deposits (Merey & Sinayuc, 2016). The presence of gas hydrates in the Danube fan, located in the western part of the Black Sea, is inferred from the identification of a hydrate-related seismic reflector called the bottom-simulating reflector (BSR). The BSR corresponds to a decrease in the seismic impedance between a hydrate-bearing sediment characterized by a high *P* wave velocity and a gas-charged layer characterized by a low *P* wave velocity. The BSR occurs at the limit of gas hydrate stability, which depends on the pressure, temperature, salinity conditions, and gas composition (Holbrook et al., 1996; Shipley et al., 1979). BSRs may present various forms such as a reverse polarity, they may be semicontinuous, or show aligned terminations of high amplitudes (Davies et al., 2017). The BSR has been mapped out in the western Black Sea by Popescu et al. (2007) who also indicate the presence of multiple BSRs in the Danube deep-sea fan (Popescu et al., 2006) that could be related to past stability conditions (Zander et al., 2017).

In addition to BSR identification, gas seeps and gas-related seismic evidences have been also reported in the Danube fan (Popescu et al., 2007). Methane seepages are widespread on the shelf and on the slope of the Black Sea especially along the Ukrainian (Greinert et al., 2010; Naudts et al., 2006, 2009) and Romanian margins (Popescu et al., 2007). More recently, Riboulot et al. (2017) identified more than 1,400 gas seeps in the Romanian sector of the Black Sea based on water column acoustic records. Gas emissions in the water column seem to be controlled by the geomorphology and gas hydrates extent as 98% of the gas seeps are located in a water depth where gas hydrates are thermodynamically unstable. Consequently, the presence of hydrate seems to prevent any free gas migration into the sediments and the water column. It has to be highlighted that a large number of seeps observed by Riboulot et al. (2018) are located close to the predicted landward termination of the gas hydrate stability zone (GHSZ) and where hydrates could be currently under destabilization related to the salt diffusion within the sediment (Riboulot et al., 2018).

The present study aims at providing a comprehensive understanding of the gas hydrate system of the Romanian margin (Figure 1) by assessing the following questions: (1) how hydrate deposits are

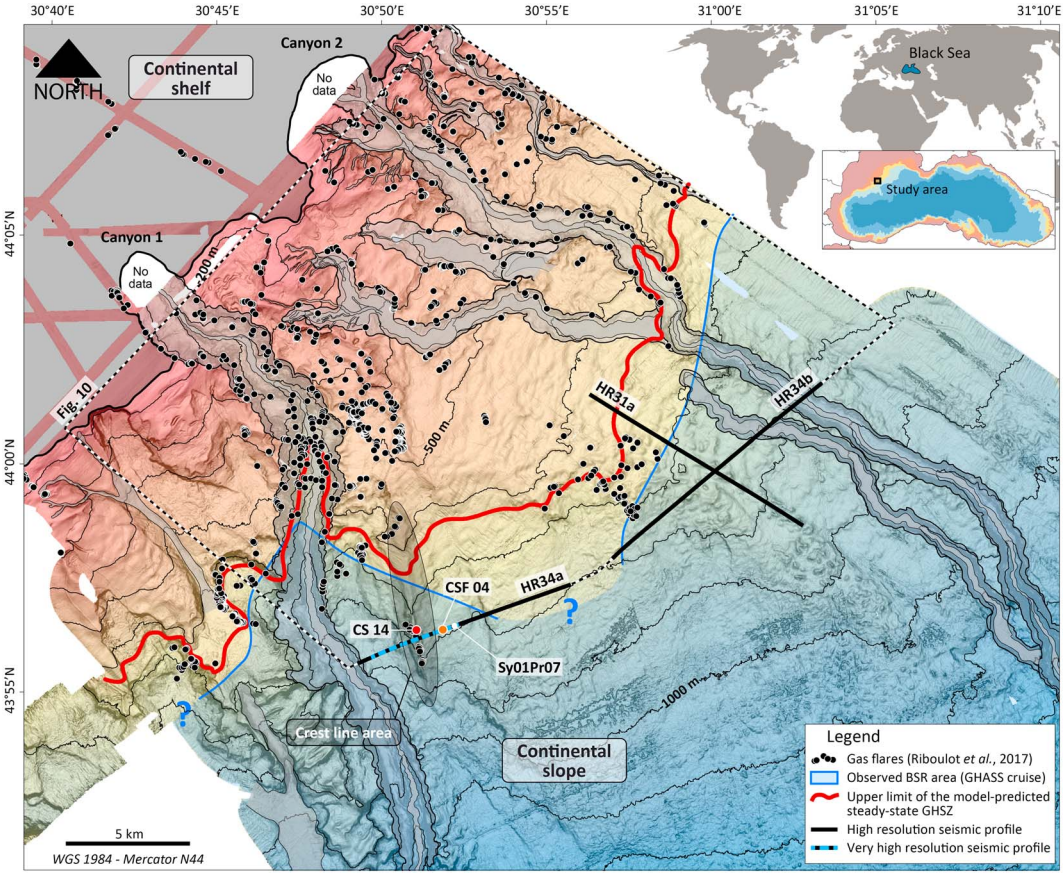

Figure 1. Bathymetric map of the study area with location of the high-resolution (HR) and very high resolution (Sy01Pr07) seismic profiles and with superposed BSR area (modified from Popescu et al., 2007 using the results obtained in this study). The BSR is not ubiquitous in the study area, but the extension of the area without BSR is unknown. The upper limit of the predicted base of the gas hydrate stability zone (BGHSZ) is indicated by the thick red line. Acoustic gas flares (black dots) are mostly located outside the gas hydrate stability zone (GHSZ) but can also be found at the landward termination of the GHSZ and within the GHSZ in the crest line area. CSF04: geothermal gradient measurement. CS14: core with gas hydrate. BSR = bottom-simulating reflector.

distributed within the GHSZ? (2) where hydrate deposits impede the vertical migration of free gas and how to explain the presence of gas flares within the GHSZ? and (3) what is the current dynamics of the hydrate system? Characterization of the gas hydrate system is performed using an integrated analysis of geophysical data acquired during the 2015 Gas Hydrates, fluid Activities and Sediment deformations in the western Black Sea (GHASS) cruise (doi:10.17600/15000500) on board the R/V *Pourquoi Pas?*. The acquired data set includes multibeam bathymetric and water column data, 2D high-resolution and very high-resolution seismic reflection profiles, high-resolution *P* wave velocity fields, and modeling of the base of GHSZ (BGHSZ). We use the BSR to define the BGHSZ as it marks a sharp border between hydrate deposit and free gas. The vertical extent of hydrate-bearing sediments is revealed by positive *P* wave velocity anomalies. Gas-related seismic signatures and low velocity enable to identify the distribution of free gas within Black Sea marine sediments. To complete the quantitative characterization of the hydrate system, we estimate methane and hydrate concentrations from *P* wave velocity inversion using first-principle-based effective models. Observed BSR depths are compared to predicted depths of the BGHS at present and during the Last Glacial Maximum (LGM) in steady state conditions by using well-constrained parameters from in situ measurements and literature.

2. The Study Area

The study area is located in the Romanian margin northward and close to the Danube canyon between 150- and 1,000-m water depth (Figure 1). The margin is characterized by a shelf edge occurring at 190-m water

depth and a continental slope with a mean value of 2° (Riboulot et al., 2017). The outer shelf and the slope are incised by two canyons and are affected by seafloor instabilities identified through headwall scarps. Water column acoustic records acquired during the GHASS cruise enable to map the distribution of 1,409 gas seeps (Riboulot et al., 2017). Ninety-eight percent of gas flares are located between 200- and 700-m water depth. Gas flare locations can be associated to canyons, headwall scarps, pockmarks, or the landward termination of the current predicted GHSZ indicated by the thick red line in Figure 1. The 2% remaining gas flares are localized within the GHSZ, along a crest line that could be related to a fault system similar to what has been observed at the Blake ridge crest by Gorman et al. (2002).

3. Data and Methods

3.1. High-Resolution Surface Seismic Data

To undertake a comprehensive study of the free gas/gas hydrate system, several HR seismic profiles were acquired perpendicular to the slope in order to investigate the transition between the domain outside the GHSZ from the upper slope (550- to 650-m water depth) down to the deeper slope within the GHSZ (800–900 m of water depth). Two additional HR seismic profiles (HR34a and HR34b) were acquired within the GHSZ. The profile H34a was localized perpendicular to the crest line area where acoustic flares occurred with the aim to understand the mechanism controlling the presence of free gas within the GHSZ. The joint analysis of high-resolution velocity analysis and prestack depth migration seismic data realized on these profiles provides an effective tool for characterizing hydrate systems (Crutchley et al., 2015; Sarkar et al., 2012) or defining the internal structure of hydrate-related chimney (Plaza-Faverola et al., 2010).

Two-dimensional high-resolution seismic profiles were acquired using a 96-channel streamer (Sentinel® solid technology) of 6.25-m group intervals and a maximum source-receiver offset of 650 m. The seismic source consisted of a single small air gun (min-GI© 24 cubic inches) providing a short repeatable signature. The streamer was towed at a depth of 2 m, while the air gun was deployed at 1.5 m. The resulting source signal has a 40–170 Hz frequency bandwidth with a central frequency of 110 Hz.

For the whole seismic data set (including profile H34b presented in Figure 2b), we applied a conventional poststack processing sequence. Detailed Root Mean Square (RMS) velocity analyses were performed on super gathers every 150 m (5 combined Common Mid Point (CMP) every 24 CMPs) corresponding to the lateral resolution of the resulting velocity field. The picking of RMS velocities was performed on semblance panels using a horizon consistent approach. Interval velocities were computed using Dix's law. The 2D velocity model was then smoothed in order to compute Green's functions used to perform the poststack depth Kirchhoff migration.

For two profiles of particular interest (HR31a and HR34a presented in Figures 2a and 2c), we processed the seismic data by using a prestack depth imaging sequence. The first step of the sequence involves the determination of the velocity field. We use a migration velocity analysis (MVA) procedure that is based on iterative prestack Kirchhoff depth migration using a layer-stripping method (Al-Yahya, 1989; Marsset et al., 2012). The principle of this seismic imaging procedure is to compare migration results obtained for a range of velocities at given locations called common image gathers (CIG). The determination of the velocity is driven by focalizing, at the same depth of reflection, amplitudes associated with a different range of offsets. Detailed velocity analyses were performed on CIG every 32 m corresponding to the lateral resolution on the velocity field. The depth interval 2D velocity model is built using a layer stripping approach. For a given layer, the updated velocity is the one that best focused the bottom reflector. Velocity within a layer is vertically constant but varies laterally. In order to avoid unrealistic lateral variations, the velocity is edited and smoothed along the layer by giving higher weight to CIG of clear focalization and by maintaining trends. To allow sharp velocity contrast at the BSR, layers with pinch-outs are allowed. The selection of horizons/layers is driven both by geophysical and geological constraints. Green's functions used to perform the Kirchhoff prestack depth migration are obtained with the Eikonal equation solver (Podvin & Lecomte, 1991). The second step of the sequence is to perform the prestack depth migration by using the velocity model obtained by the velocity analysis procedure. Seismic resolutions after migration are in the order of 3.5 m vertically and 15 m horizontally (mean seismic wavelength). Related to the sensitivity in the velocity picking and to the edition step, uncertainties on *P* wave velocity are estimated to be ±50 m/s up to the depth of 1,000 m and increase to ±100 m/s at 1,200 m using MVA approach. The conventional analysis provides *P*

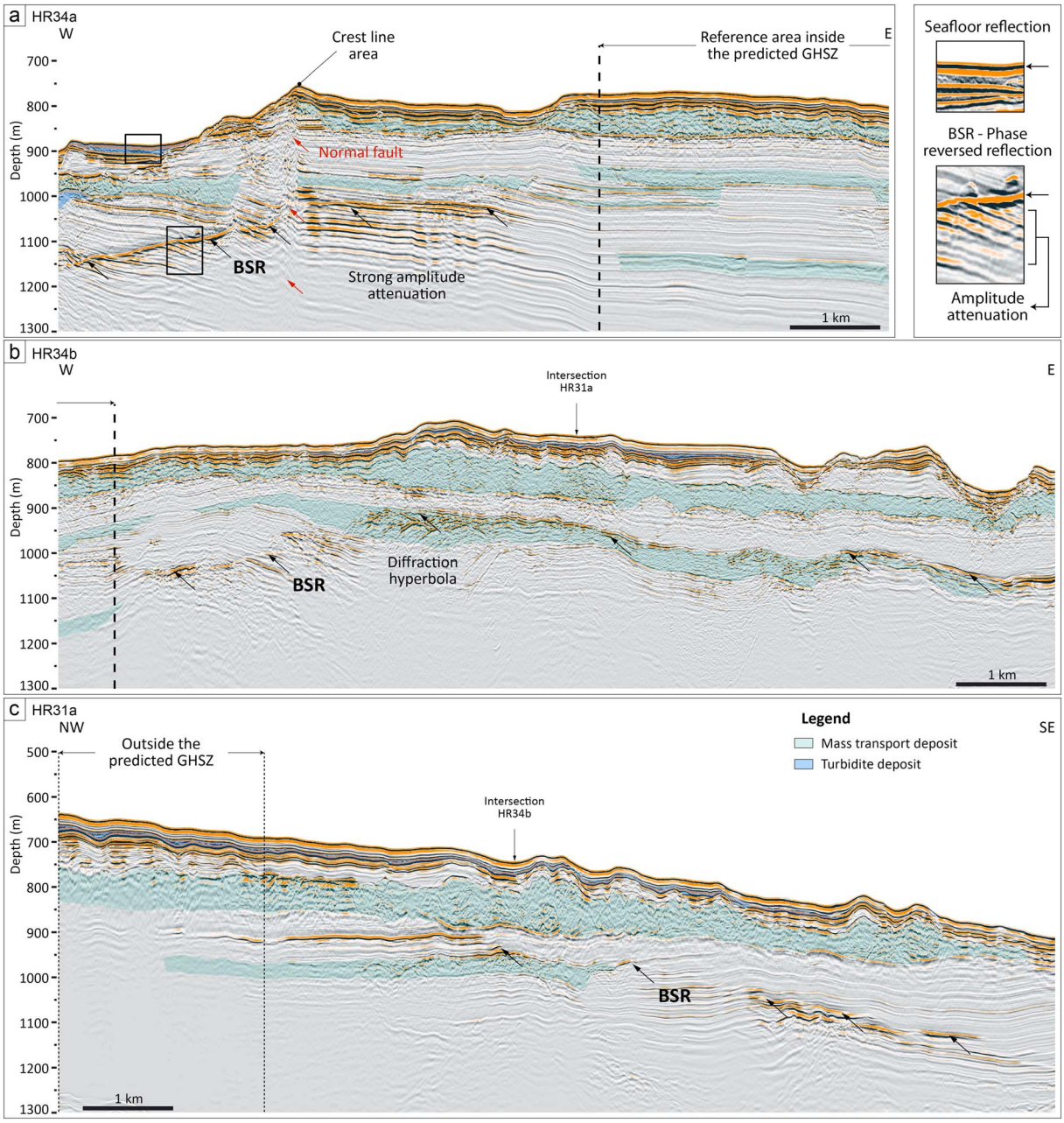

Figure 2. High-resolution seismic profiles: (a) HR34a, (b) HR34b both located within the GHSZ, and (c) HR31a that crosses the landward termination of the GHSZ. BSR (thick black dashed line) is ubiquitous within the GHSZ except in the so-called *reference area* located at the eastern part of profile HR34a. The onset indicates the reverse polarity of the BSR related to the seafloor reflection and the amplitude attenuation right under the BSR due to the presence of free gas. Mainly three seismic facies can be identified: (1) low-amplitude subparallel seismic reflectors related to hemipelagic sediments, (2) low-amplitude seismic facies related to turbidites (in blue), and (3) chaotic facies associated with mass transport deposit (in green). BSR = bottom-simulating reflector; GHSZ = gas hydrate stability zone.

wave velocity values with greater uncertainties, which are estimated to be twice those of the MVA analysis. Data penetration is limited to 500 mbsf (meter below sea floor) related to the presence of gas and the high-frequency content of seismic data.

3.2. Deep-Towed Seismic Data

Two-dimensional very high resolution deep-towed seismic profiles were acquired with the Ifremer SYstème SIsmique Fond system (Marsset et al., 2014). SYstème SIsmique Fond is a deep-towed seismic device hosting a Janus-Helmholtz transducer emitting a linear chirp signal in the frequency bandwidth (220–1050 Hz) and

a 52-channel seismic streamer with a hydrophone spacing of 2 m, both towed between 50 and 100 m above the seafloor. After careful processing of the positioning, seismic signature deconvolution enables to obtain a 1-m vertical resolution while the prestack depth imaging procedure specifically developed for the particular geometry of the deep-towed acquisition (Marsset et al., 2014, 2018) allows to reach a 2-m lateral resolution.

3.3. In Situ Measurements and Cores

During the GHASS cruise, in situ measurements and cores were collected. Geochemical measurements performed on gas hydrate samples, which were collected for the first time in the Romanian sector of the Black Sea, confirmed that the gas entrapped is biogenic methane with a concentration of 99.6% (Riboulot et al., 2018), and the remaining 0.4% is mainly N_2. Pore water analyses performed on eight cores revealed a gradual fall in salinity from 22 psu at the seafloor level to near 2 psu at around 25 mbsf. A mineralogy analysis performed on eight cores up to 30-m deep below the seafloor indicated that the average composition of these soft sediments is made of 60% clay, 35% quartz, and 5% calcite (Ballas et al., 2018).

3.4. Estimates of Gas Hydrate and Methane Concentration

Regarding the lack of borehole data to precisely define an effective medium model taking into account gas hydrate morphology and free gas distribution, we used first principle-based effective medium models to obtain rough estimates of gas hydrate and methane concentrations. For gas hydrate, we used the upper and lower bounds of the Helgerud et al. (1999) effective medium model, which either consider hydrate as part of the pore space or part of the sediment frame. For methane, we used the model of White et al. (1975) as it accounts for the attenuation of the high frequencies clearly observed on the seismic data. This model considers a patchy distribution of free gas using a periodic layered system composed of porous media; the attenuation comes from wave-induced fluid flow (WIFF). This phenomenon, which cannot exist in the case of a homogeneous gas distribution, occurs at a mesoscopic scale where the size of the gas pocket is much larger than the pore size but lower than the seismic wavelength (Müller et al., 2010). Using attenuation-related quantities as the Q value in addition to P wave velocity enables to derive (1) the gas concentration in the range defined by the Gassmann-Wood and Gassmann-Hill bounds (Carcione & Picotti, 2006) and (2) the mean size of gas patches. This joint inversion of Q and P wave velocity was conducted where robust Q measurements (i.e., not affected by scattering attenuation due to complex wave propagation) were derived from HR data using the centroïd frequency shift method (Ker & Le, 2018; Quan & Harris, 1997).

3.5. Base of Gas Hydrate Stability Zone Modeling

The BGHSZ has been computed in steady state conditions. We consider a pure s-I methane hydrate as the main component of gas from the Black Sea hydrates is biogenic methane (99.6% from our geochemical measurements and 93.3–99.7% for the whole Black Sea from Vassilev & Dimitrov, 2003). The stability of methane hydrate is controlled by the following parameters: (1) pore pressure that is given by the hydrostatic condition with a gradient of 10 kPa/m, (2) temperature that is 8.9 °C at the seafloor and increases with depth with a geothermal gradient of 24.5 °C/km (CSF04, Figure 1; Riboulot et al., 2018), (3) salinity is derived from the measured chloride profile over 25 m below the seafloor (mbsf) that decreases from 22 psu at the seafloor to 2 psu at 25 mbsf (Riboulot et al., 2018) and then remains constant down to 400 mbsf (Calvert & Batchelor, 1978).

We also computed the predicted BGHSZ for past conditions during the LGM period (Constantinescu et al., 2015). The sea level reached a low value down to −100/−150 m (Demirbağ et al., 1999; Winguth et al., 2000), and the seawater temperature at the seafloor was estimated to be 4 °C by Soulet et al. (2011). As the Black Sea was a lake, the salinity of the sediment pore water was constant with a value of 2 psu down to 400 mbsf. The GHSZ was simulated using the two-dimensional GH stability model developed by Sultan et al. (2010), in order to take into account the bathymetry profile.

4. Results

4.1. Seismic Observations: Stratigraphy, BSR, and Gas-Related Reflections

4.1.1. Stratigraphy

Three main kinds of seismic facies can be identified on seismic profiles presented in Figure 2: (1) low-amplitude subparallel seismic reflectors related to hemipelagic layers, (2) low-amplitude/transparent seismic facies (in gray) related to small turbidity deposits less than 20-m thick. and (3) low-amplitude chaotic

seismic facies with distinctive internal high amplitude associated with mass transport deposits (in light green). A buried mass transport deposit (MTD) is identified on all seismic profiles acquired to the east of Canyon 1 (Figure 2). The extension of this MTD is limited to the north by the shelf edge and to the east by the crest line. The top of this MTD is found at various depths below the seafloor from 50 to 100 m, and its thickness varies from 20 to 120 m and has an increasing trend seaward and in its eastward extension. Several other MTDs are present on the study area at larger depth below the seafloor but with a lower lateral extension.

Below the crest line area (Figure 2a), a splay of faults can be observed separating subparallel layers and affecting the imaged sedimentary column. Faults termination could not be identified due to a lack of penetration of the seismic signal. At the location of the crest and in its vicinity, large gas flares up to 400-m high rising from the seafloor were detected through water column acoustics. Acoustic signatures of gas flares are superimposed on a deep-towed seismic profile acquired along the same track as profile HR34a in Figure 3. Hydrate samples were collected near the gas flares indicating the coexistence of free gas and gas hydrates within sediments close to the seafloor.

4.1.2. BSR Distribution

Indirect evidence of gas hydrate is related to BSR observation. The BSR identified on HR seismic profiles is mainly characterized by a reversal of the wave polarity compared to the reflection at the seafloor as presented in the close-up of Figure 2a. The BSR can also present aligned terminations of high amplitudes (HR31a and HR34b). The BSR is ubiquitous over the study area except in the eastern part of HR34a. The BSR is indicated by dashed thick lines on the three profiles of Figure 2, and the BSR spatial extent is shown by the blue line in Figure 1. The new acquired seismic data have enabled to update the Popescu et al. (2007) map of the BSR distribution with a more accurate depth location (related to the depth imaging procedure that has been performed). The seaward extension of the area without BSR was not identified.

4.1.3. Gas-Related Reflections

Below the BSR, the presence of free gas is revealed by high-amplitude reflections and high attenuation of the frequency content (close-up of Figure 2). In shallow water depth, outside the GHSZ (Figure 2c), gas-related seismic signatures such as bright spot or velocity pull-down artifact can be observed above the main MTD. In the eastern part of HR34a inside the GHSZ (Figure 2a), no anomalous seismic signature associated with free gas has been identified in the whole sedimentary column.

4.2. Velocity Anomalies as Proxies of Hydrate and Gas Occurrence

4.2.1. Profile HR34a

The eastside of the profile (i.e. the *reference area* in Figure 4a that shows neither evidence of BSR nor gas) exhibits a gentle increase of velocity with depth. The westside of the profile shows a different distribution of the velocity with depth as a velocity inversion (i.e., a sharp decrease of velocity) can be observed precisely at the location of the BSR: high interval velocity (1,700–2,050 m/s) above the BSR and low interval velocity (1,200–1,500 m/s) below the BSR. Consequently, compared to the velocity values measured in the absence of BSR (reference area), positive and negative velocity anomalies exist on either side of the BSR. As the BSR corresponds to the limit of stability of gas hydrates, it can be assessed with high confidence that the high interval velocity (1,700–2,050 m/s) is related to the presence of gas hydrate-bearing sediments and the low interval velocity (1,200–1,500 m/s) is related to free gas-bearing sediments. The highest velocity (2,050 m/s) is observed at the west side of the crest. East of the crest, the positive velocity anomalies, although characterized by lower values, also indicate that the presence of gas hydrate is very likely. The vertical extension of a positive anomaly layer related to hydrate deposit could reach a thickness of 200 m west of the crest, whereas it is limited to a maximum of 100 m to the east.

Low-velocity anomalies observed below the BSR correlated with the decrease in frequency content strongly indicate the presence of free gas. A 30-m thick layer below the shallowest BSR is characterized by the lowest velocity of ~1,200 m/s**.** The maximum offset of the seismic data is too short to constrain through velocity analysis the base of the free gas zone under the BSR.

4.2.2. Profile HR31a

Likewise the seismic profile HR34a, a strong velocity inversion is associated with the presence of the BSR that is located in the southern side of profile HR31a (Figure 4c). A zone of high velocity (1,900–2,050 m/s)

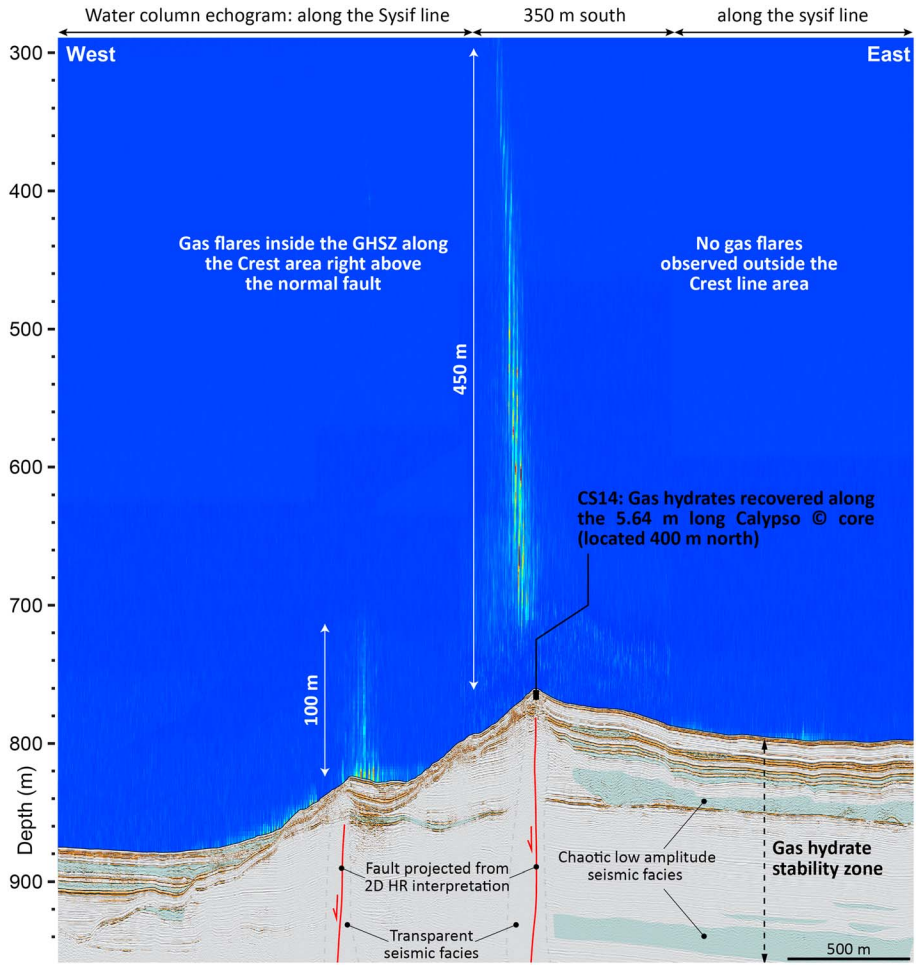

Figure 3. The processed water column echogram along the Sysif line PL01PR07 shows the location of two gas flares above the two vertical discontinuities in the crest line area inside the GHSZ. The acoustic signature of the gas flare has a height of ~400 m. The hydrate samples collected in the vicinity of the crest line area (core CS14) indicate the nature of the gas that is mostly methane (99.6%). Presence of hydrate in the superficial sediment and of free gas in the water column in this area shows the coexistence of free gas and hydrate in the GHSZ. GHSZ = gas hydrate stability zone.

is localized just above the BSR and under a MTD characterized by a *P* wave velocity of about 1,750 m/s. This high-velocity zone is associated with the presence of GH within sediments. Under the BSR, the velocity is low and highly variable laterally with *P* wave velocities ranging from 1,200 to 1,600 m/s. The trend of the velocity is to decrease as the BSR goes deeper toward the southern part of the profile. Outside the GHSZ, in the northern part of the profile, a succession of velocity inversions can be observed related to the obvious presence of free gas (Figure 2c, e.g., bright spots above the MTD).

4.2.3. Profile HR34b

High-resolution velocity analysis cannot be undertaken on the HR34b profile due to the strong 3D nature of the subseafloor, responsible for diffractions and out of plane reflections, and a lack of coherent seismic horizons necessary to perform the MVA approach. We thus applied a conventional approach with a lower resolution and a higher uncertainty but sufficient to detect the main trend of the *P* wave velocity. Dots on the velocity field of the HR34b profile (Figure 4b) indicate the reflection points picked for the semblance analysis that is not fully horizon consistent. A velocity inversion is visible on the whole profile except at the western border, which belongs to the reference area. The thickness of the high-velocity layer above the BSR is about 50 to 100 m. It should be noted that the discrepancy in velocity values at the intersection of profile HR31a is mainly related to the lack of resolution of the conventional approach and to a higher uncertainty related to the high structural complexity of the subseafloor, especially related to the MTD.

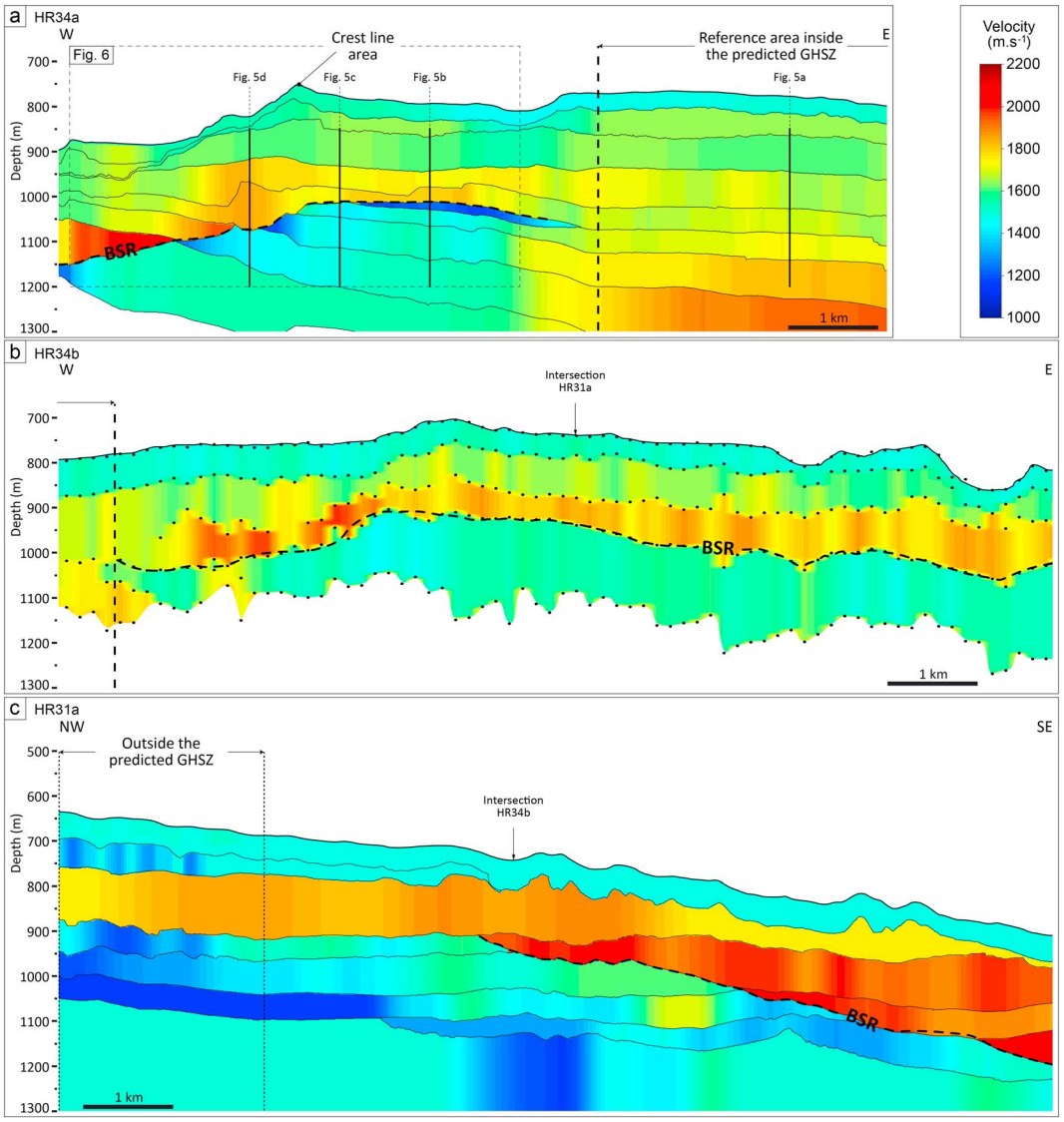

Figure 4. Interval *P* wave velocity field inferred from high-resolution seismic profiles: (a) HR34a, (b) HR34b, and (c) HR 31a. The velocity analysis was performed using a migration velocity analysis for profiles HR34a and HR31a and a conventional NMO approach for profile HR34b. High velocity associated with gas hydrates can be observed just above the BSR with a vertical extension of ~50 to 200 m. Low velocity located under the BSR relates the presence of free gas. The locations of four vertical velocity profiles are indicated on profile HR34a (a): one profile within the reference area, three profiles crossing the velocity inversion related to the BSR (b–d).

4.3. Hydrate and Gas Volumetric Concentration

Estimating hydrate and free gas concentration from effective medium theory requires first to determine a background velocity model for the marine sediments within the studied area. As the reference area presented in Figure 2 appears to be free of gas and gas hydrates, it is a suitable location to determine the reference *P* wave background velocity by calibrating an effective medium model for normally consolidated marine sediments. Mineralogy analyses realized on cores (Ballas et al., 2018) and borehole data available from DSP Leg 42 at site 380 (Calvert & Batchelor, 1978) show that the upper sediments of the Black Sea are mainly composed of clay (60–65%) and quartz (30–35%) and in a smaller proportion calcite (5–10%). In the reference area, the *P* wave velocity derived from seismic data is characterized by a linear gradient of 0.68 s^{-1} that is controlled by the decrease in porosity with depth (Figure 5a dashed blue curve). The inversion of the observed velocity gradient, based on the effective medium model from Dvorkin et al. (1999) and

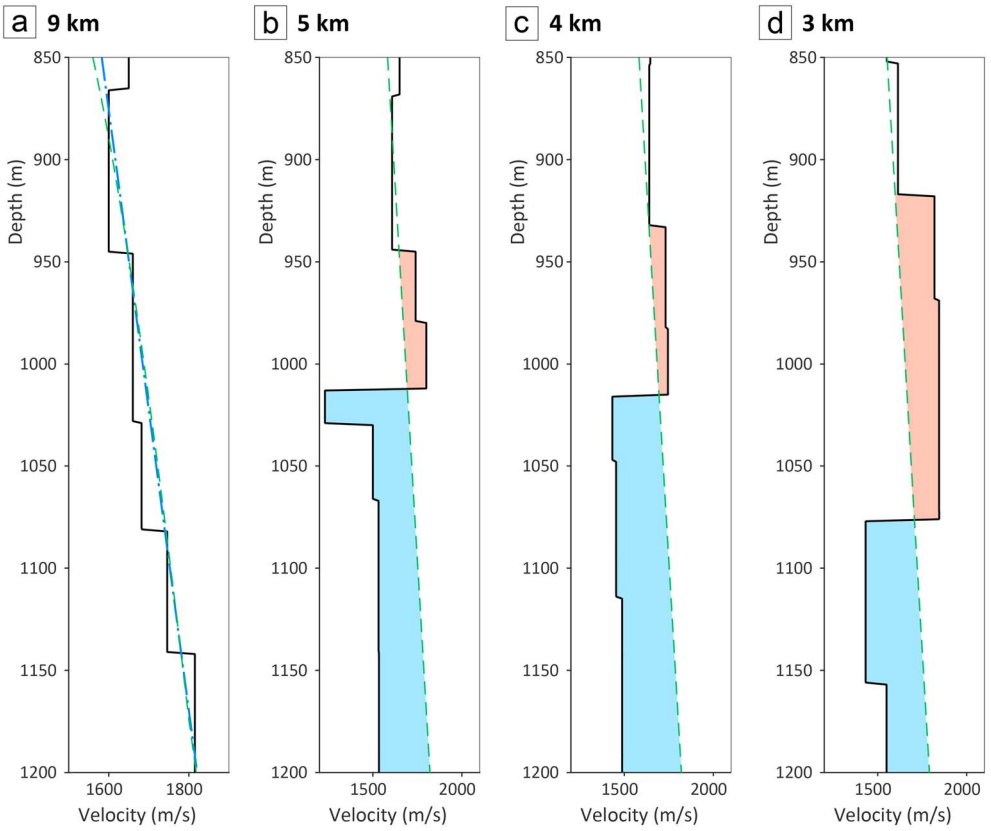

Figure 5. Vertical *P* wave velocity profiles extracted from the velocity field of the HR34a profile. (a) A profile within the reference area (black line), linear velocity gradient representative of the velocity behavior of the reference area (dash-dotted blue line), (b) background velocity (green dashed line) best fitting the linear gradient using effective medium model-based inversion enabling to determine the depth porosity variation. (c and d) Velocity profiles showing positive velocity anomalies (in red) compared to background velocity related to gas hydrates and negative velocity anomalies (in blue) related to free gas.

on the mineralogy defined above, enables to determine the initial void ratio ($e_0 = 4.4$) and the compression index ($C_c = 0.58$) that control the evolution of porosity with the effective stress (or depth) in agreement with Terzaghi's theory (Terzaghi et al., 1996). Based on the deviation to the background velocity (green curves in Figures 5a–5d), we determine positive (red filled area) and negative (blue filled area) velocity anomalies that are used to determine gas hydrate and gas concentration, respectively. Figures 6a and 6b present hydrate volumetric concentrations related to load-bearing and pore-filling hydrate models (Helgerud et al., 1999) inferred from the velocity field of the western part of the profile HR34a. Figure 6c presents the gas volumetric concentration obtained by inversion of *P* wave velocity using the WIFF model from White et al. (1975). A mean size of gas patches of 2 m for the WIFF model was determined by a joint inversion of *P* wave velocity and *Q* value in the area at the eastside of the crest where attenuation could be confidently measured ($Q = 35 \pm 5$). Uncertainties, related to *P* wave velocity, *Q* factor estimates, and poroelastic parameters, were used to quantify a relative error of 30% on gas hydrate and methane volumetric concentrations.

Significant positive velocity anomalies are limited to layers lying just above the BSR. The hydrate concentration has an average value of 5% or 10% considering either the load-bearing or the pore-filling hydrate models. Maximum hydrate concentration is located on the western side of the profile HR34a (15%–22%, Figures 6a and 6b). Negative velocity anomalies under the BSR are related to gas volumetric concentrations of 4–6% except for the upper gas layer where the concentration may reach 12% (Figure 6c). As the uncertainty is about 30%, lateral variation of hydrate or gas concentration has to be cautiously interpreted.

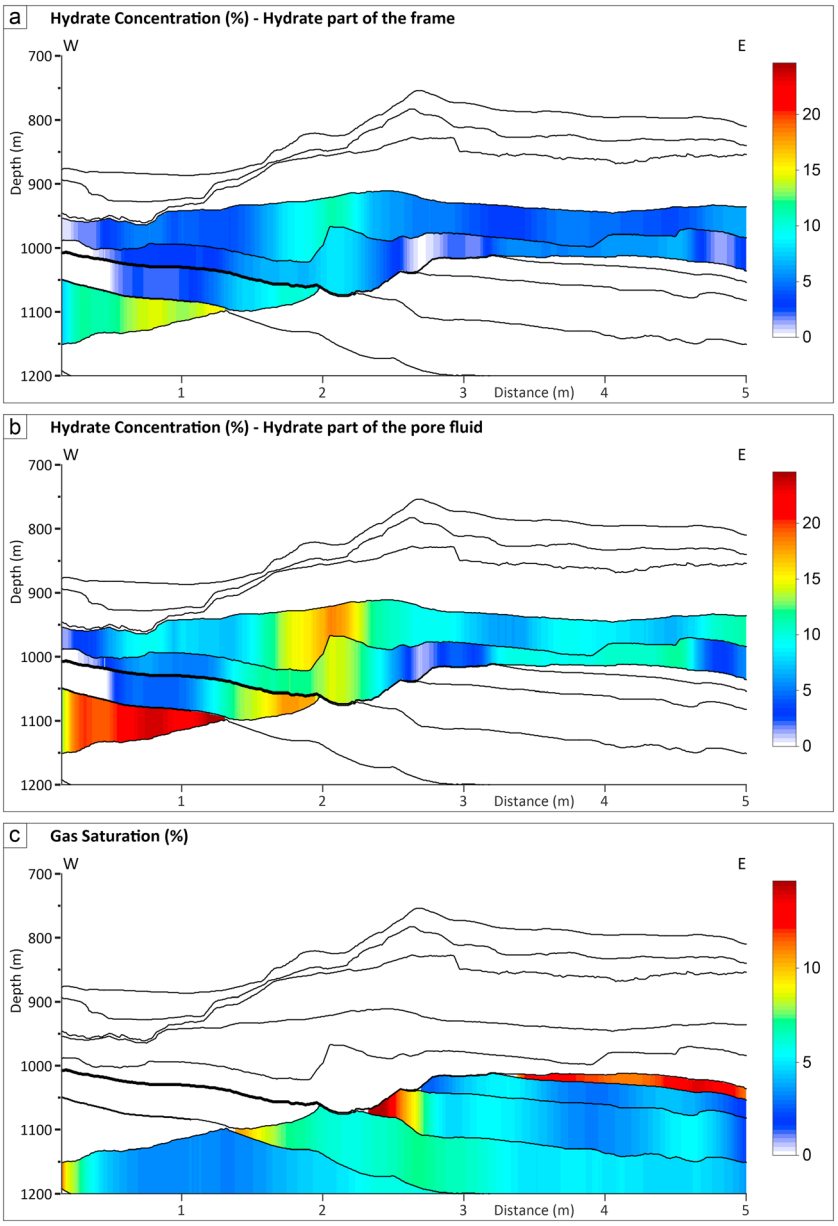

Figure 6. Hydrate volumetric concentration inferred from positive *P* wave velocity anomalies of profile HR34a using effective medium theory (Helgerud et al., 1999): Hydrate considered as part of the frame (a) or as part of the pore fluid (b). (c) Gas volumetric concentration obtained from negative *P* wave velocity anomalies and attenuation quantity (*Q*) using the White et al. (1975) model.

4.4. Results of BGHSZ Modeling

Figure 7 presents the predicted steady state BGHSZ associated with past (LGM) and present conditions for seismic profiles HR34a and HR31a (Figures 7a and 7c, and 7b and 7d respectively). The predicted steady state paleo-BGHSZ related to the LGM is deeper than the current one for both considered LGM conditions of −150 and −100 m for the sea level and a seafloor temperature of 4 °C. The depth of the paleo-BGHSZ associated with the LGM reveals that the thickness of the GHSZ could have been substantially higher than the current one (Figures 7a and 7b). The predicted steady state BGHSZ at present differs from the observed BSR location for both profiles HR34a and HR31a (Figures 7c and 7d, respectively). The BSR depth is located between the deeper-predicted paleo-BGHS and the shallower-predicted BGHS although closer to the present BGHS.

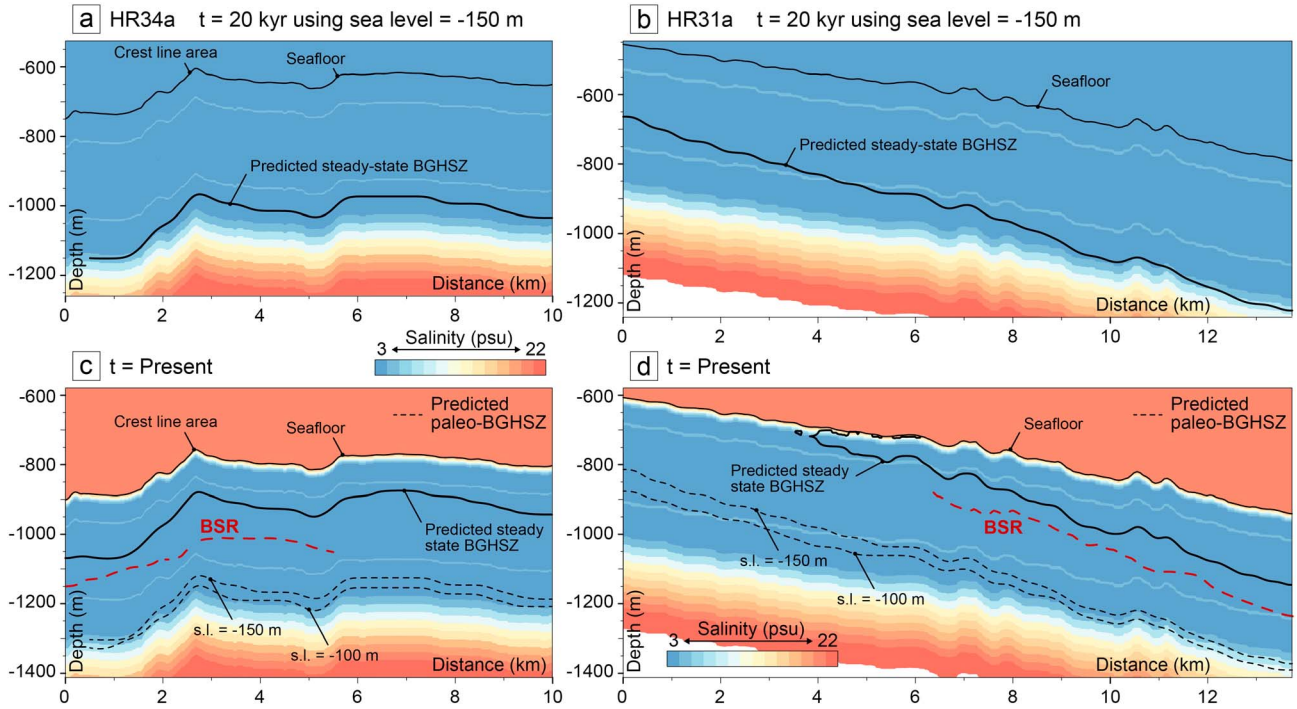

Figure 7. (a and b) Model-predicted steady state BGHS for seismic profiles HR34a and HR31a during the LGM assuming a sea level 150 m below the present sea level. Salinity of sediment pore water is derived from cores for the subsurface and from DSDP hole 379A for the deeper section. Temperature at the seafloor is 8.9 °C at present time and was 4 °C during the LGM; geothermal gradient is 24.5 °C/km. The GHSZ was thicker than at present. (c and d) Predicted BGHS at present (thick black line) and during LGM (dashed line) and observed BSR depths for both HR34a and HR31a profiles. A discrepancy between observed BSR and current predicted BGHSZ is observed. The observed BSR is located between the past and current predicted BGHSZ. GHSZ = gas hydrate stability zone; BGHSZ = base of the gas hydrate stability zone; LGM = Last Glacial Maximum; DSDP = Deep Sea Drilling Project; BSR = bottom-simulating reflector.

5. Discussion

5.1. Hydrates as a Barrier for Gas Migration

The BSR marks the BGHSZ as it corresponds to the interface between high-velocity hydrate-bearing sediments and low-velocity free gas-bearing sediments. The high velocity layer above the BSR is related to the presence of hydrate with a significant volumetric concentration (5–10%). The location of these hydrate deposits is limited to the lower part of the GHSZ close to the BSR with a variable thickness that does not exceed 50–100 m at the landward termination and increases seaward (200 m for the deepest water depth of seismic profile HR31a). Gas hydrates could be present in the upper part of the GHSZ but with a very low concentration (< 2%) as no significant increase in velocity was observed.

Free gas occurrence is ubiquitous below the BSR as indicated by the drop in *P* wave velocity and outside the GHSZ where it can be observed close to the seafloor from gas-related signatures and low-velocity zones (Figure 8c). Outside the GHSZ, the free gas can migrate up to the seafloor and escapes into the water column and generates gas flares (Riboulot et al., 2017). Within the GHSZ, gas flux from deeper sources is converted to hydrates, which impede the upward vertical gas migration by reducing the permeability of marine sediments. This result is in accordance with theoretical (Nimblett & Ruppel, 2003) and experimental investigations (Chuan-Hui et al., 2014; Johnson et al., 2011) attesting a permeability reduction by 1 to 2 orders of magnitude related to the presence of hydrates.

It has to be highlighted that within the reference area where no BSR is observed, neither positive nor negative velocity anomalies were detected as well as no gas-related seismic signatures. In this area, the lack of gas migration path prevents the gas reaching the upper part of the sedimentary column and forming gas hydrates.

The fact that the GHSZ acts as a permeability barrier for gas migrating from deeper sediments into the water column is a well-known process (Ginsburg & Soloviev, 1997; Naudts et al., 2006). However, this study

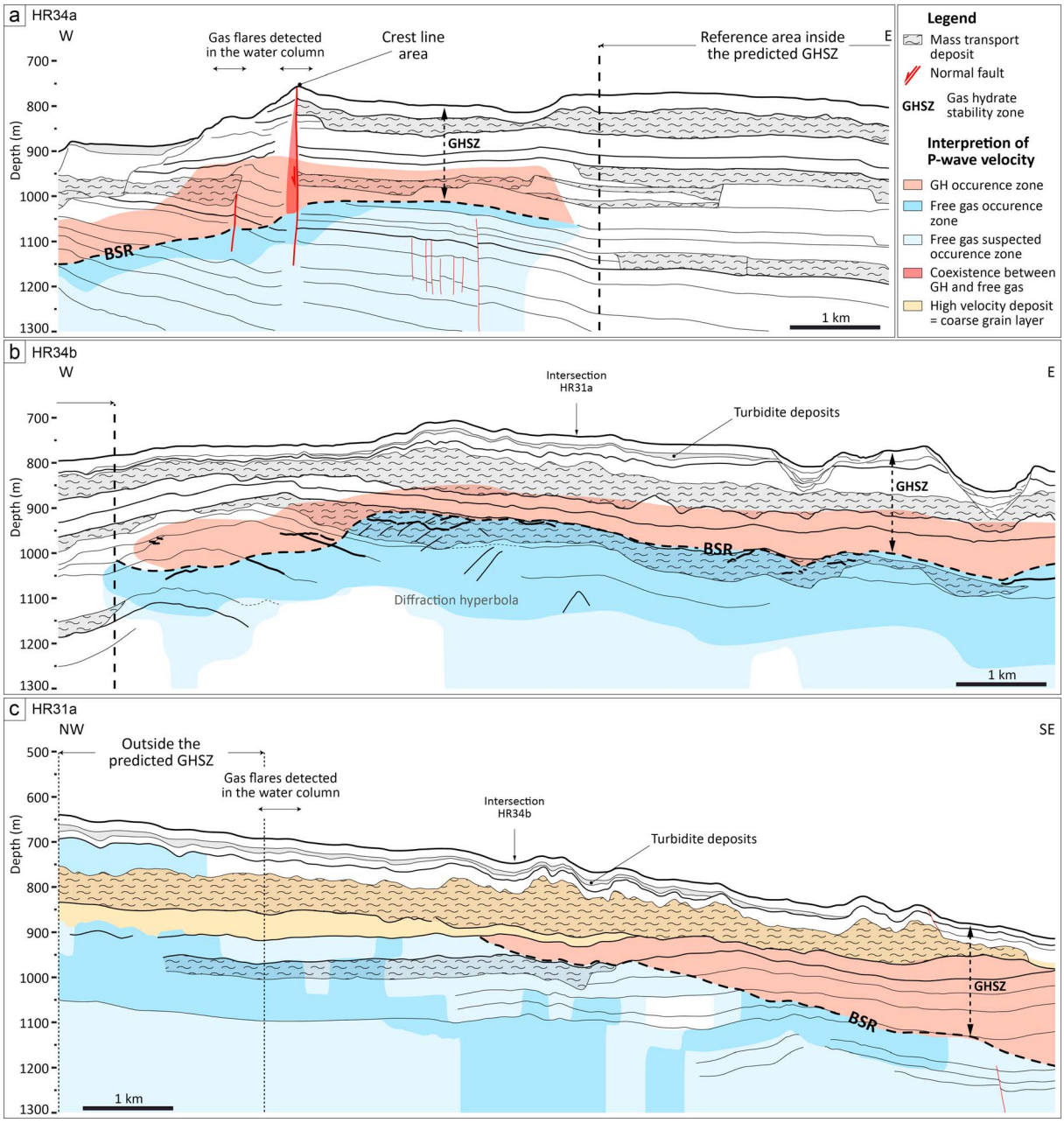

Figure 8. Interpreted seismic profiles (a) HR 34a, (b) HR34b, and (c) HR31a showing hydrate deposits (in red) and the free gas occurrence zone (in blue). Hydrate deposits are located close to the BSR with a vertical extension up to 50–200 m. BSR (bold dash line) is located between model-predicted steady state BGHS at present and during the LGM. On profile HR34a (Figure 8a), the BSR is only located in the western part of the profile. The fault system above the crest line is characterized by the coexistence between gas hydrates and free gas. BSR = bottom-simulating reflector; GHSZ = gas hydrate stability zone; LGM = Last Glacial Maximum.

enables to establish that an ~50- to 100-m thick deposit of hydrate located close to the BSR with a volumetric concentration of 5–10% is sufficient to clog the system and prevent upward free-gas migration.

5.2. Transient State of the Gas Hydrate System

We note a discrepancy between computed BGHSZ and observed BSR depth with a misfit up to 100 m (Figures 7c and 7d). Previous studies focused on investigating the cause of BGHSZ/BSR mismatch on different margins (Flemings et al., 2003; Hornbach et al., 2004; Plaza-Faverola et al., 2017; Xu & Ruppel, 1999).

Phrampus et al. (2014), for instance, observed a similar phenomenon on the upper U.S. Beaufort margin, and the discrepancy was mainly attributed to significant warming of intermediate ocean temperatures.

For the case of the Western Black Sea, we explore four main hypotheses that may explain that the observed BSRs is deeper than the predicted steady state BGHSZ:

1. different composition of gas or water than the ones measured in situ and used in the calculation of the thermodynamic stability of gas hydrates (Dickens & Quinby-Hunt, 1997; Plaza-Faverola et al., 2017; Popescu et al., 2006),
2. inaccurate geothermal gradient values and possible spatial variation (Grevemeyer & Villinger, 2001; Minshull & Keddie, 2010; Yamano et al., 1982),
3. a transient state of the hydrate system related to the nonequilibrium of the thermal regime (Phrampus et al., 2014), and
4. a transient state of the hydrate system related to the excess pore pressure generated by hydrate dissociation.

Phrampus et al. (2014) investigated other phenomena to explain anomalously deep BSR observed on the upper U.S. Beaufort margin as erosion/sedimentation effects and uplift, but these processes are not relevant to our study area of the Romanian margin. Indeed, the sediment rate in the studied zone presented here is 14 cm/kyr, so the most recent unit since the end of the LGM is about 2-m thick (forthcoming publication). This sedimentation rate is in agreement with the one of Soulet et al. (2011) calculated on a core 20 km northeast of our zone by 350-m water depth. The mass transport complexes detected on seismic data are older than the LGM. The sedimentation has no effect on the evolution of the GHSZ since the LGM.

1. *Difference in gas or water composition*. The gas composition was obtained by analysis of gas hydrate samples from the upper part of the hydrate stability zone in the vicinity of a fault system (crest line area, Figure 1), allowing the migration of free gas through the GHSZ. The hydrates formed in the first 6 m of sediment below the seafloor entrapped biogenic methane accumulated under the BGHS. We consider that the gas entrapped in recovered hydrates is representative of the gas composition related to this sector of the Black Sea. The pore water composition is freshwater 25 m below the seafloor down to 400 m (Deep Sea Drilling Project hole 379A). Consequently, difference in gas or water composition is unlikely to be responsible for the discrepancy between observed BSR and computed BGHSZ.
2. *The nonequilibrium of the thermal regime*. Poort et al. (2005) show a transient state of the thermal regime in the whole Black Sea following the LGM. In order to assess if the thermal regime is in a transient state or at equilibrium in the study area, we perform 1D modeling based on the resolution of the differential equation governing the temperature variation down to 350 m below the seafloor. The initial temperature is set at 4 °C at the seafloor at the moment of the connection between the Black and the Mediterranean Seas (9 kyr before present; Soulet et al., 2011). The present temperature of the water is 8.9 °C. We use a range of values for the thermal diffusivity of marine sediments from $1 \cdot 10^{-7}$ to $5 \cdot 10^{-7}$ m^2/s. We do not consider the presence of gas hydrates in our modeling. The evolution of the temperature with depth computed for a seafloor at 800-m water depth is shown in Figure 9. The thermal modeling shows that the temperature equilibrium has been reached since 2 or 3 kyr before present for the lowest thermal diffusivity. Despite seafloor temperature changes since the LGM or 9 kyr ago, we consider that the thermal readjustment is complete and does not impact on the current GHSZ.
3. *The value of the geothermal gradient and its possible spatial variability*. We perform the inversion of the geothermal gradient for the seismic profiles HR34a and HR31a by matching the modeled BGHSZ and observed BSR depth. Figures 10a and 10b present the derived spatial variations of the geothermal gradient inverted along both seismic profiles. We take into account uncertainties on depth locations (due to *P* wave velocity uncertainties) to evaluate the uncertainty on the geothermal gradient (gray area) that can reach 0.5 °C/km. Figures 10c and 10d present the statistical distribution of inverted geothermal gradients. For the seismic profile HR34a, the range of variations is very large (16–24 °C/km) with an occurrence peak at 19.5 °C/km. The lowest value at 16 °C/km occurs at the location of the fault system right above the crest area. For the seismic profile HR31a, the range of variation is narrower (17.5–21.5 °C/km) with an occurrence peak at 20.5 °C/km. These inversion results indicate that a geothermal gradient value of ~20 °C/km could enable a better fit with the current depth of the observed BSR compared to the one of 24.5 ± 0.2 °C/km used for the modeling and derived from in situ

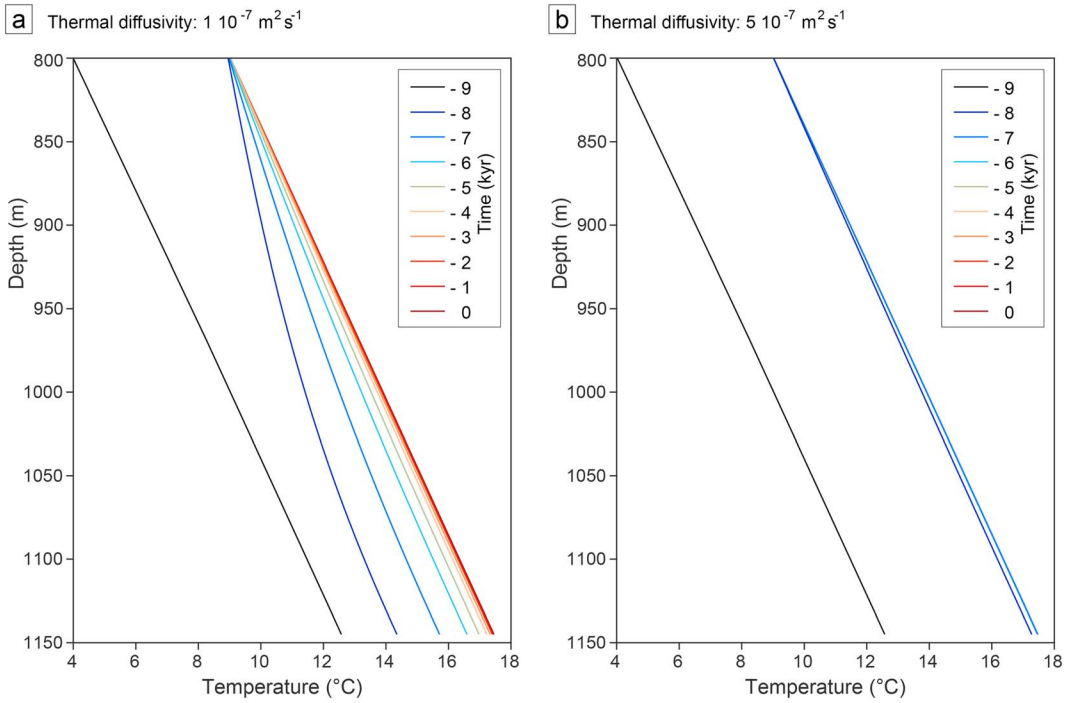

Figure 9. One-dimensional modeling of the temperature variation below the seafloor (800-m water depth) during the last 9 kyr. The initial temperature is 4 °C at the seafloor at the moment of the connection between the Black and the Mediterranean Seas (9 kyr before present). The present temperature of the water is 8.9 °C. The modeling was performed using two values for the thermal diffusivity of marine sediments: $1 \cdot 10^{-7}$ (a) and $5 \cdot 10^{-7}$ m^2/s (b).

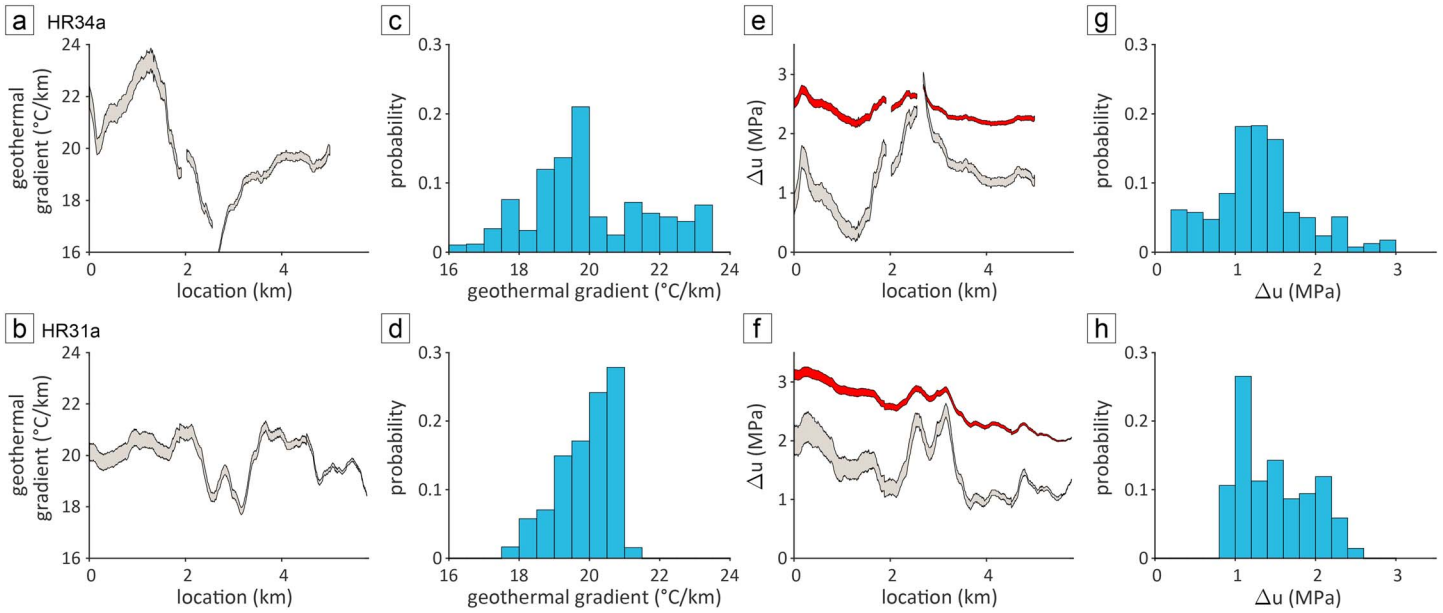

Figure 10. Lateral variation (a, b, e, and f) and statistical (c, d, g, and h) distribution of inferred geothermal gradient (°C/km) and maximum excess pore pressure Δu (MPa) from BSR depth for seismic profiles HR34a and HR31a, respectively. The gray area represents the uncertainty in geothermal gradient and Δu estimates associated with the uncertainty in BSR depth. The red area in Figures 10e and 10f represents the effective stress with its uncertainty. BSR = bottom-simulating reflector.

measurements (Riboulot et al., 2018). However, a geothermal gradient of 20 °C/km would make the observed BSR above the predicted steady state BGHS in numerous locations on both seismic profiles. A possible mechanism responsible for such BSR depth anomalies is difficult to argue. The very large range of variations (up to 8 °C/km) appears to be very unlikely in such a short distance of 2 km. Indeed, the nature of the subseafloor allows to exclude rapid lateral variation of marine sediment thermal conductivity. Furthermore, the presence of methane hydrate can be neglected when considering first-order thermal conductivity (Waite et al., 2009). Lastly, the geothermal gradient might be affected by rising warm fluid at the crest location connected to the deeper part of the basin by a fault system, but instead of high geothermal gradient values, the lowest values of profile HR34a are obtained.

4. Excess pore pressure due to the migration of the BGHS over recent geological history. Overpressure conditions in the free-gas zone right under the BGHS could lead to form hydrate below the theoretical thermodynamic conditions (Tinivella & Giustiniani, 2013). But, as the observed BSR depth is located between the current and the LGM predicted steady state BGHS, we suppose that the gas hydrate layer formed right above the BGHS during the LGM is brought outside the stability conditions when sea level and seafloor temperature rise. The modification of the general gas hydrate thermodynamic conditions generates gas hydrate dissociation producing a free gas/water mixture that will increase pore pressure. Sultan (2007a, 2007ab) showed that before reaching a reequilibrium, the hydrate system is in a transient regime in which excess pore pressure generated by hydrate dissociation enables the recrystallization of part of the hydrate and delays the hydrate dissociation process. This phenomenon produces a metastable thermodynamic state where gas and gas hydrates coexist. The upper bound of excess pore pressure Δu can be estimated from the difference between the hydrate equilibrium pressure corresponding to the temperature at the current BSR depth and the pressure at the current BSR depth (Sultan, 2007b). We use this approach to derive Δu for both seismic profiles by using a constant geothermal gradient of 24.5 °C/km and by taking into account uncertainty in BSR depths. The spatial variation is displayed in Figures 10e and 10f. The statistical distribution of Δu is presented in Figures 10g and 10h. As the inverted Δu depends on BSR depth, its spatial distribution is anticorrelated with the one of the inverted geothermal gradient. The uncertainty in Δu can reach up to 0.5 MPa, but the mean uncertainty is 0.2 MPa. For HR34a, the maximum pore pressure varies in the range (0.26–3 MPa) with a peak occurrence at 1.2 MPa. The highest values of Δu (2–3 MPa) are located above the crest line area and are close to the effective stress values (in red). For HR31a, the maximum pore pressure varies in the range (0.8–2.5 MPa) with a peak occurrence at 1.1 MPa. Δu values are almost everywhere lower than 80% of the effective stress values (in red).

The lateral variation of inverted excess pore pressure could be related to variation in hydrate-bearing sediment permeability. High hydrate concentration may imply low permeability of sediments and high Δu values. Δu values of ~3 MPa at the crest line area could generate the required hydrofracturing process allowing to break hydrates located inside the fault and permitting the upward fluid migration emerging at the seafloor. This high excess pressure may not be only related to hydrate dissociation but also to free-gas accumulation coming from deeper reservoirs.

An Δu value of about 1–2 MPa may indicate the efficiency of gas hydrates to lower the fluid circulation capacity of the system. Such high Δu values may explain why the current state of the hydrate system has not yet reached a steady state as the pressure reequilibrium is a long term process (as an example, a dissipation of 0.5 MPa takes about 10 kyr at 200 bsf and a permeability of 10^{-9} m^2). This phenomenon appears to be a self-preserving behavior of gas hydrates that impedes the hydrate system dissociation. The impact of this high excess pore pressure exceeding at the same locations as 70% of the vertical effective stress is expected to drastically reduce sediment stability and could be the source of some of the observed landslides in the area.

5.3. Main Mechanisms Controlling the Evolution of the Hydrate System

In Figure 11, we propose a schematic hydrate system view to represent the main observed features offshore the western Black Sea and the mechanisms controlling its evolution.

1. The hydrate system is characterized by a dynamic transient regime at the top of the GHSZ related to change in salinity of sediment pore water since the reconnection between the Mediterranean and Black Seas, which generates a migration of the landward termination of the GHSZ (Riboulot et al., 2018). The GHSZ also migrates upward in response to past temperature and sea level changes since

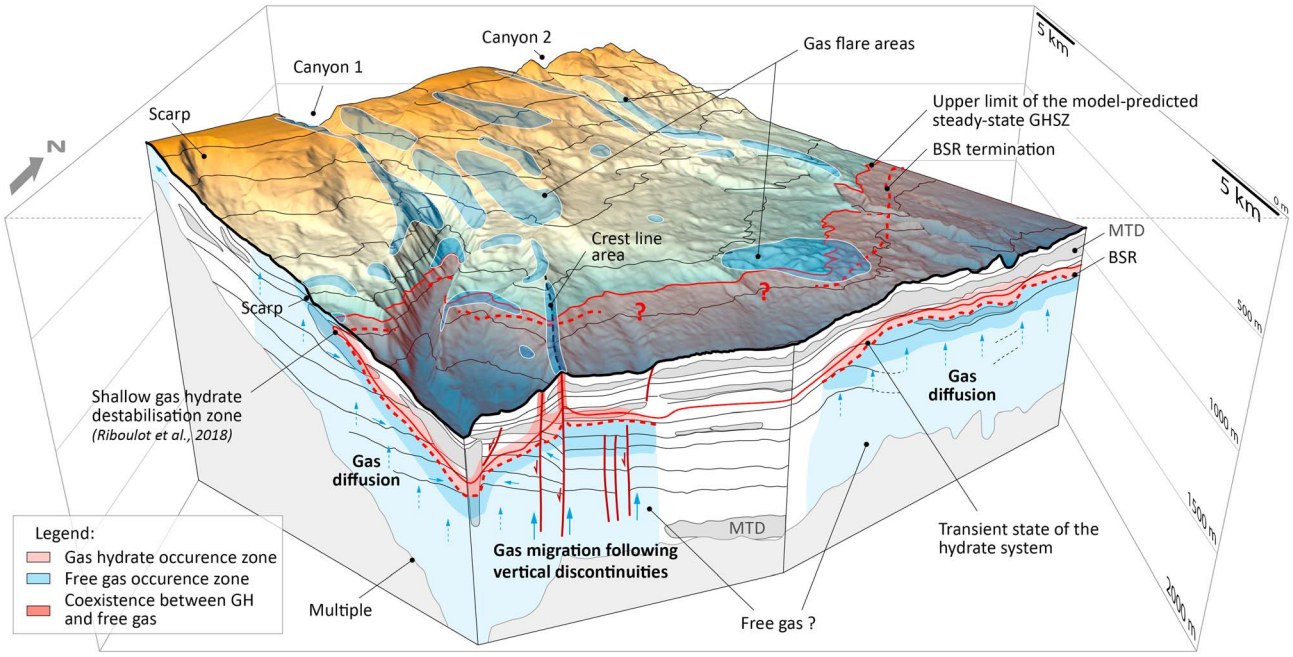

Figure 11. Three-dimensional interpretative view of the hydrate system of the Romanian margin. Gas hydrate deposits with significant concentrations (5–10%) are located in the lower part of the GHSZ with a vertical extension of 50–200 m. Hydrate deposits impede the upward migration of free gas coming from a deeper part of the margin. Gas flares observed at the seafloor inside the GHSZ are located at the crest line connected to a fault system enabling gas migration and the coexistence with gas hydrates. The hydrate system is currently in transient state associated with (1) a migration of the BGHS related to a reequilibrium in response to the evolution of controlling factors of gas hydrate stability since the Last Glacial Maximum (this study) and (2) a migration of the landward termination related to the salinization of sediments (Riboulot et al., 2018). GHSZ = gas hydrate stability zone.

the LGM (Figure 7), a mechanism highlighted by Ruppel and Kessler (2017). This upward migration could be slowed down by excess pore pressure associated with hydrate dissociation explaining an anomalously deep BSR.

2. The hydrate-bearing sediment system is dominated by a concentration of 5–10% (light red, Figure 11) that clogs the upward gas migration. Outside the GHSZ, the free gas reaches the seafloor producing a large number of gas flares in the water column (dashed blue arrows). In the GHSZ, under the BGHSZ, sedimentary layers are characterized by the absence of discontinuities and vertical gas migration pathways although locally disturbed in the crest area by a fault system. The accumulation of free gas under the BGHS is interpreted as the result of a long lasting process dominated by gas diffusion.
3. Locally, hydrofracturing produced by excess pore pressure associated with hydrate dissociation and free-gas supply from deeper reservoirs enables a significant flux of free gas to cross the GHSZ by using preexisting faults in the crest area and reach the seafloor producing free-gas seepages within the hydrate stability zone. In the crest line area, hydrate nodules were sampled at shallow depths (< 10 m) below the seafloor. The fault system is thus characterized by the coexistence of free gas and gas hydrates (dark red area, Figure 11).

6. Conclusion

Based on the integrated analysis of geophysical data and modeling of GHSZ, we show the following.

1. The occurrence of hydrate deposits with a volumetric concentration of 5–10% limited to the lower part of the GHSZ with a mean thickness of 50–100 m reduces sediment permeability and prevents upward free-gas migration by clogging the fluid system in the GHSZ.
2. The observed leakages escaping from the gas hydrate barrier are related to excess pore pressure enabling the free gas to cross the GHSZ and reach the seafloor at the crest line area by using a preexisting fault system. This fault system is characterized by the coexistence of free gas and hydrates.

3. A discrepancy exists between observed BSR and model-predicted steady state BGHSZ. The observed BSR depth is located between the depths of both present and past predicted steady state BGHSZ. The shift in BSR depth could be mainly the result of a current transient state of the hydrate system related to excess pore pressure localized at the BGHSZ due to gas hydrate dissociation as thermodynamic conditions have changed since the LGM. This excess pore pressure enables the recrystallization of hydrate delaying the system in reaching equilibrium and is expected to drastically reduce sediment stability and could be the source of some of the observed landslides in the area.
4. The BSR, which is commonly used as a proxy to derive geothermal gradient values in steady state conditions, could be used to derive maximum excess pore pressure of 1–2 MPa at the BGHSZ when it is in transient state.

While gas hydrate systems have been recognized and described worldwide, we show through this multidisciplinary study the complexity of having a comprehensive view of hydrate dynamics over time without considering all the intrinsic parameters involved in the formation and evolution of gas hydrates.

Acknowledgments
The support by officers and crew during the GHASS cruise on board R/V *Pourquoi Pas?* (2015) is greatly appreciated, as is the dedication of the Genavir and Ifremer technical staff during the cruise. We thank Andreia Plaza Faverola and an anonymous reviewer for their comments that help us to improve this paper. We thank sincerely Alison Chalm and Shane Murphy for the revision of the English language. We thank L. Ruffine for insightful discussion. Data sets used in the current study are acquired during the GHASS expedition (10.17600/15000500), and data set information are available in the GHASS cruise report (http://archimer.ifremer.fr/doc/00300/41141). Data are available from the SISMER website (http://data.ifremer.fr).

References

Al-Yahya, K. (1989). Velocity analysis by iterative profile migration. *Geophysics*, *54*(6), 718–729. https://doi.org/10.1190/1.1442699

Ballas, G., Garziglia, S., Sultan, N., Pelleter, E., Toucanne, S., Marsset, T., et al. (2018). Influence of early diagenesis on geotechnical properties of clay sediments (Romania, Black Sea). *Engineering Geology*, *240*, 175–188. https://doi.org/10.1016/j.enggeo.2018.04.019

Calvert, S. E., & Batchelor, C. H. (1978). *Major and minor element geochemistry of sediments from Hole 379A, Leg 42B, Deep-Sea Drilling Project, Initial Reports of the Deep Sea Drilling Project* (Vol. 42, pp. 527–541). Washington, DC: Government Printing Office.

Carcione, J. M., & Picotti, S. (2006). P-wave seismic attenuation by slow-wave diffusion: Effects of inhomogeneous rock properties. *Geophysics*, *71*(3), O1–O8. https://doi.org/10.1190/1.2194512

Chuan-Hui, L., Qian, Z., Hong-Jun, X., Kai, F., & Xue-Wei, L. (2014). Relation between relative permeability and hydrate saturation in Shenhu area, South China Sea. *Applied Geophysics*, *11*, 207–214.

Constantinescu, A. M., Toucanne, S., Dennielou, B., Jorry, S. J., Mulder, T., & Lericolais, G. (2015). Evolution of the Danube deep-sea fan since the Last Glacial Maximum: New insights into Black Sea water-level fluctuations. *Marine Geology*, *367*, 50–68. https://doi.org/10.1016/j.margeo.2015.05.007

Crutchley, G. J., Fraser, D. R. A., Pecher, I. A., Gorman, A. R., Maslen, G., & Henrys, S. A. (2015). Gas migration into gas hydrate-bearing sediments on the southern Hikurangi margin of New Zealand. *Journal of Geophysical Research: Solid Earth*, *120*, 725–743. https://doi.org/10.1002/2014JB011503

Davies, R. J., Morales Maqueda, M. A., Li, A., & Ganopolski, A. (2017). Millennial-scale shifts in the methane hydrate stability zone due to Quaternary climate change. *Geology*, *45*(11), 1027–1030. https://doi.org/10.1130/G39611.1

Demirbağ, E., Gökaşan, E., Oktay, F. Y., Simsek, M., & Yüce, H. (1999). The last sea level changes in the Black Sea: Evidence from seismic data. *Marine Geology*, *157*(3-4), 249–265. https://doi.org/10.1016/S0025-3227(98)00158-3

Dickens, G. R., & Quinby-Hunt, M. S. (1997). Methane hydrate stability in pore water; a simple theoretical approach for geophysical applications. *Journal of Geophysical Research*, *102*(B1), 773–783. https://doi.org/10.1029/96JB02941

Dvorkin, J., Prasad, M., Sakai, A., & Lavoie, D. (1999). Elasticity of marine sediments. *Geophysical Research Letters*, *26*(12), 1781–1784. https://doi.org/10.1029/1999GL900332

Flemings, P. B., Liu, X., & Winters, W. J. (2003). Critical pressure and multiphase flow in Blake ridge gas hydrates. *Geology*, *31*(12), 1057–1060. https://doi.org/10.1130/G19863.1

Ginsburg, G. D. (1998). Gas hydrate accumulation in deep-water marine sediments. *Geological Society, London, Special Publications*, *137*(1), 51–62. https://doi.org/10.1144/GSL.SP.1998.137.01.04

Ginsburg, G. D., & Soloviev, V. A. (1997). Methane migration within the submarine gas-hydrate stability zone under deep-water conditions. *Marine Geology*, *137*(1-2), 49–57. https://doi.org/10.1016/S0025-3227(96)00078-3

Gorman, A. R., Holbrook, W. S., Hornbach, M. J., Hackwith, K. L., Lizarralde, D., & Pecher, I. (2002). Migration of methane gas through the hydrate stability zone in a low-flux hydrate province. *Geology*, *30*(4), 327–330. https://doi.org/10.1130/0091-7613(2002)030<0327:MOMGTT>2.0.CO;2

Greinert, J., McGinnis, D. F., Naudts, L., Linke, P., & De Batist, M. (2010). Atmospheric methane flux from bubbling seeps: Spatially extrapolated quantification from a Black Sea shelf area. *Journal of Geophysical Research*, *115*, C01002. https://doi.org/10.1029/2009JC005381

Grevemeyer, I., & Villinger, H. (2001). Gas hydrate stability and the assessment of heat flow through continental margins. *Geophysical Journal International*, *145*(3), 647–660. https://doi.org/10.1046/j.0956-540x.2001.01404.x

Helgerud, M. B., Dvorkin, J., Nur, A., Sakai, A., & Collett, T. (1999). Elastic-wave velocity in marine sediments with gas hydrates—Effective medium modeling. *Geophysical Research Letters*, *26*(13), 2021–2024. https://doi.org/10.1029/1999GL900421

Holbrook, W. S., Hoskins, H., Wood, W. T., Stephen, R. A., & Lizarralde, D. (1996). Methane hydrate and free gas on the Blake ridge from vertical seismic profiling. *Science*, *273*(5283), 1840–1843. https://doi.org/10.1126/science.273.5283.1840

Hornbach, M. J., Saffer, D. M., & Holbrook, W. S. (2004). Critically pressured free-gas reservoirs below gas-hydrate provinces. *Nature*, *427*(6970), 142–144. https://doi.org/10.1038/nature02172

Johnson, A., Patil, S., & Dandekar, A. (2011). Experimental investigation of gas-water relative permeability for gas-hydrate bearing sediments from the Mount Elbert gas hydrate stratigraphic test well, Alaska north slope. *Marine and Petroleum Geology*, *28*(2), 419–426. https://doi.org/10.1016/j.marpetgeo.2009.10.013

Ker, S., & Le Gonidec, Y. (2018). Fractional integration of seismic wavelets in anelastic media to recover multiscale properties of impedance discontinuities. *Geophysics*, *83*(2), V61–V71. https://doi.org/10.1190/geo2017-0527.1

Marsset, B., Ker, S., Thomas, Y., & Colin, F. (2018). Deep-towed high resolution seismic imaging II: Determination of P-wave velocity distribution. *Deep Sea Research: Part I-Oceanographic Research Paper*, *132*, 29–36.

Marsset, B., Menut, E., Ker, S., Thomas, Y., Regnault, J. -P., Leon, P., et al. (2014). Deep-towed high resolution multichannel seismic imaging. *Deep Sea Research Part I: Oceanographic Research Paper*, *93*, 83–90.

Marsset, B., Thomas, Y., Sultan, N., Gaillot, A., & Stephan, Y. (2012). A multi-disciplinary approach to marine shallow geohazard assessment. *Near Surface Geophysics*, *10*(4), 279–288. https://doi.org/10.3997/1873-0604.2012012

Merey, S., & Sinayuc, C. (2016). Investigation of gas hydrate potential of the Black Sea and modelling of gas production from a hypothetical class 1 methane hydrate reservoir in the Black Sea conditions. *Journal of Natural Gas Science and Engineering*, *29*, 66–79. https://doi.org/10.1016/j.jngse.2015.12.048

Minshull, T. A., & Keddie, A. (2010). Measuring the geotherm with gas hydrate bottom-simulating reflectors: A novel approach using three dimensional seismic data from the eastern Black Sea. *Terra Nova*, *22*(2), 131–136. https://doi.org/10.1111/j.1365-3121.2010.00926.x

Müller, T., Gurevich, B., & Lebedev, M. (2010). Seismic wave attenuation and dispersion resulting from wave-induced flow in porous rock—A review. *Geophysics*, *75*(5), 75A147–75A164.

Naudts, L., De Batist, M., Greinert, J., & Artemov, Y. (2009). Geo-and hydroacoustic manifestations of shallow gas and gas seeps in the Dnepr paleodelta, northwestern Black Sea. *The Leading Edge*, *28*(9), 1030–1040. https://doi.org/10.1190/1.3236372

Naudts, L., Greinert, J., Artemov, Y., Staelens, P., Poort, J., Van Rensbergen, P., & De Batist, M. (2006). Geological and morphological setting of 2778 methane seeps in the Dnepr paleo-delta, northwestern Black Sea. *Marine Geology*, *227*, 177–199.

Nimblett, J., & Ruppel, C. (2003). Permeability evolution during the formation of gas hydrates in marine sediments. *Journal of Geophysical Research*, *108*(B9), 2420. https://doi.org/10.1029/2001JB001650

Phrampus, B. J., Hornbach, M. J., Ruppel, C. D., & Hart, P. E. (2014). Widespread gas hydrate instability on the upper U.S. Beaufort margin. *Journal of Geophysical Research: Solid Earth*, *119*, 8594–8609. https://doi.org/10.1002/2014JB011290

Plaza-Faverola, A., Vadakkepuliyambatta, S., Hong, W.-L., Mienert, J., Bünz, S., Chand, S., & Greinert, J. (2017). Bottom simulating reflector dynamics at Arctic thermogenic gas provinces: An example from Vestnesa ridge, offshore west Svalbard. *Journal of Geophysical Research: Solid Earth*, *122*, 4089–4105. https://doi.org/10.1002/2016JB013761

Plaza-Faverola, A., Westbrook, G. K., Ker, S., Exley, J. K., Gailler, A. R., Minshull, T. A., & Broto, K. (2010). Evidence from three-dimensional seismic tomography for a substantial accumulation of gas hydrate in a fluid-escape chimney in the Nyegga pockmark field, offshore Norway. *Journal of Geophysical Research*, *115*, B08104. https://doi.org/10.1029/2009JB007078

Podvin, P., & Lecomte, I. (1991). Finite difference computation of traveltimes in very contrasted velocity models. A massively parallel approach and its associated tools. *Geophysical Journal International*, *105*(1), 271–284. https://doi.org/10.1111/j.1365-246X.1991.tb03461.x

Poort, J., Vassilev, A., & Dimitrov, L. (2005). Did postglacial catastrophic flooding trigger massive changes in the Black Sea gas hydrate reservoir? *Terra Nova*, *17*(2), 135–140. https://doi.org/10.1111/j.1365-3121.2005.00599.x

Popescu, I., De Batist, M., Lericolais, G., Nouzé, H., Poort, J., Panin, N., et al. (2006). Multiple bottom-simulating reflections in the Black Sea: Potential proxies of past climate conditions. *Marine Geology*, *227*(3-4), 163–176. https://doi.org/10.1016/j.margeo.2005.12.006

Popescu, I., Lericolais, G., Panin, N., De Batist, M., & Gillet, H. (2007). Seismic expression of gas and gas hydrates across the western Black Sea. *Geo-Marine Letters*, *27*(2-4), 173–183. https://doi.org/10.1007/s00367-007-0068-0

Quan, Y., & Harris, J. M. (1997). Seismic attenuation tomography using the frequency shift method. *Geophysics*, *62*(3), 895–905. https://doi.org/10.1190/1.1444197

Riboulot, V., Cattaneo, A., Scalabrin, C., Gaillot, A., Jouet, G., Ballas, G., et al. (2017). Control of the geomorphology and gas hydrate extent on widespread gas emissions offshore Romania. *Bulletin de la Societe Geologique de France*, *188*(26).

Riboulot, V., Ker, S., Sultan, N., Thomas, Y., Marsset, B., Scalabrin, C., et al. (2018). Freshwater lake to salt-water sea causing widespread hydrate dissociation in the Black Sea. *Nature Communications*, *9*(1). https://doi.org/10.1038/s41467-017-02271-z

Ruppel, C. D., & Kessler, J. D. (2017). The interaction of climate change and methane hydrates. *Reviews of Geophysics*, *55*, 126–168. https://doi.org/10.1002/2016RG000534

Sarkar, S., Berndt, C., Minshull, T. A., Westbrook, G. K., Klaeschen, D., Masson, D., et al. (2012). Seismic evidence for shallow gas-escape features associated with a retreating gas hydrate zone offshore west Svalbard. *Journal of Geophysical Research*, *117*, B09102. https://doi.org/10.1029/2011JB009126

Shipley, T. H., Houston, M. H., Buffler, R. T., Shaub, F. J., McMillen, K. J., Ladd, J. W., & Lamar Worzel, J. (1979). Seismic evidence for widespread possible gas hydrate horizons on continental slopes and rises. *AAPG Bulletin*, *63*, 2204–2213.

Soulet, G., Ménot, G., Lericolais, G., & Bard, E. (2011). A revised calendar age for the last reconnection of the Black Sea to the global ocean. *Quaternary Science Reviews*, *30*(9-10), 1019–1026. https://doi.org/10.1016/j.quascirev.2011.03.001

Sultan, N. (2007a). Excess pore pressure and slope failures resulting from gas-hydrates dissociation and dissolution, Offshore Technology Conference, 30 April-3 May 2007, Houston, Texas, U.S.A. ISBN 978-1-55563-254-0. OTC-18532-MS, 1–9.

Sultan, N. (2007b). Comment on "Excess pore pressure resulting from methane hydrate dissociation in marine sediments: A theoretical approach" by Wenyue Xu and Leonid N. Germanovich. *Journal of Geophysical Research*, *112*, B02103. https://doi.org/10.1029/2006JB004527

Sultan, N., Marsset, B., Ker, S., Marsset, T., Voisset, M., Vernant, A.-M., et al. (2010). Hydrate dissolution as a potential mechanism for pockmark formation in the Niger delta. *Journal of Geophysical Research*, *115*, B08101. https://doi.org/10.1029/2010JB007453

Terzaghi, K., Peck, R. B., & Mesri, G. (1996). *Soil mechanics in engineering practice* (3rd ed.p. 549). New York: John Wiley.

Tinivella, U., & Giustiniani, M. (2013). Variations in BSR depth due to gas hydrate stability versus pore pressure. *Global and Planetary Change*, *100*, 119–128. https://doi.org/10.1016/j.gloplacha.2012.10.012

Vassilev, A., & Dimitrov, L. (2003). Model evaluation of the Black Sea gas hydrates. *Annals of Bulgarian Academy of Sciences*, *56*, 3–15.

Waite, W. F., Santamarina, J. C., Cortes, D. D., Dugan, B., Espinoza, D. N., Germaine, J., et al. (2009). Physical properties of hydrate-bearing sediments. *Reviews of Geophysics*, *47*, RG4003. https://doi.org/10.1029/2008RG000279

White, J. E., Mikhaylova, N. G., & Lyakhovitskiy, F. M. (1975). Low-frequency seismic waves in fluid saturated layered rocks. Izvestija Academy of Sciences USSR. *Physics of the Solid Earth*, *11*, 654–659.

Winguth, C., Wong, H. K., Panin, N., Dinu, C., Georgescu, P., Ungureanu, G., et al. (2000). Upper Quaternary water level history and sedimentation in the northwestern Black Sea. *Marine Geology*, *167*(1-2), 127–146. https://doi.org/10.1016/S0025-3227(00)00024-4

Xu, W., & Ruppel, C. (1999). Predicting the occurrence, distribution, and evolution of methane gas hydrate in porous marine sediments. *Journal of Geophysical Research*, *104*(B3), 5081–5095. https://doi.org/10.1029/1998JB900092

Yamano, M., Uyeda, S., Aoki, Y., & Shipley, T. H. (1982). Estimates of heat flow derived from gas hydrates. *Geology*, *10*(7), 339–343. https://doi.org/10.1130/0091-7613(1982)10<339:EOHFDF>2.0.CO;2

Yefremova, A. G., & Zhizhchenko, B. P. (1974). Gas hydrate occurrences in offshore deposits. *DAN SSSR (Proceedings of the USSR Academy of Sciences)*, *214*, 1179–1181.

Zander, T., Haeckel, M., Berndt, C., Chi, W.-C., Klaucke, I., Bialas, J., et al. (2017). On the origin of multiple BSRs in the Danube deep-sea fan, Black Sea. *Earth and Planetary Science Letters*, *462*, 15–25. https://doi.org/10.1016/j.epsl.2017.01.006